

High-Frequency Electromagnetic Interference Diagnostics

Ling Zhang, Yuru Feng, Jun Fan and Er-Ping Li

Abstract

Electromagnetic interference (EMI) is becoming more troublesome in modern electronic systems due to the continuous increase of communication data rates. This chapter reviews some new methodologies for high-frequency EMI diagnostics in recent researches. Optical modules, as a typical type of gigahertz radiator, are studied in this chapter. First, the dominant radiation modules and EMI coupling paths in an explicit optical module are analyzed using simulation and measurement techniques. Correspondingly, practical mitigation approaches are proposed to suppress the radiation in real product applications. Moreover, an emission source microscopy (ESM) method, which can rapidly localize far-field radiators, is applied to diagnose multiple optical modules and identify the dominant sources. Finally, when numerous optical modules work simultaneously in a large network router, a formula based on statistical analysis can estimate the maximum far-field emission and the probability of passing electromagnetic compatibility (EMC) regulations. This chapter reviews a systematic procedure for EMI diagnostics at high frequencies, including EMI coupling path analysis and mitigation, emission source localization, and radiation estimation using statistical analysis.

Keywords: Electromagnetic interference, Emission source microscopy, Optical modules, High frequency, Industrial products

1. Introduction

Electromagnetic interference (EMI) problems are drawing more and more attention in modern electronic devices and systems. Industrial products have to satisfy electromagnetic compatibility (EMC) requirements, such as US Federal Communications Commission (FCC) regulations. However, the increase in data rate and source complexity is making EMI diagnostics more troublesome. For a sophisticated product with various potential radiation modules, investigating the root cause of radiation, main coupling paths, and practical mitigation approaches is challenging. Moreover, in a complicated system with numerous potential high-frequency radiation sources, identifying the dominant trouble-makers and quantifying the total contribution from these sources is a tedious and time-consuming process. This chapter presents a systematic procedure for high-frequency EMI diagnostics in industrial products by reviewing some recently published methodologies. As a typical high-frequency radiation source, optical modules are studied in this chapter.

First, the interior EMI coupling paths and possible mitigation methods of optical modules are studied [1–6]. The internal mechanism can be analyzed to alleviate the

radiation problem at the design stage or propose mitigation solutions. Building full-wave simulation models is a standard method to understand the behind physics. However, it is challenging to run reliable full-wave simulations for intricate structures. The adopted strategy in [1, 2] is to correlate the total radiated power (TRP) in simulation and measurement to ensure a reliable simulation model. Based on the simulation model, the EMI coupling paths are also investigated. Besides, a concept of energy parcels and their trajectories can provide a more intuitive visualization of the coupling paths. Eventually, according to the analysis result of the EMI coupling paths, mitigation solutions are proposed in both simulation and measurement to suppress the EMI coupling paths, which can effectively reduce the far-field radiation to meet EMC regulations.

For a large system with multiple radiators, identifying the dominant sources is a vital but tedious process. Near-field scanning is a standard method for EMI diagnostics [7, 8]. However, detecting near field also includes evanescent waves that do not contribute to far-field radiation. Under some circumstances, near-field probes cannot reach close enough to all locations and components due to mechanical limitations. Emission source microscopy (ESM) is a scanning technique to localize sources contributing to far-field radiation [9]. Sparse ESM [10] is an improved ESM method that identifies the dominant sources through sparse scanning samples. Therefore, sparse ESM is a more efficient method than near-field scanning to determine the main contributor for far-field radiation at high frequencies. In [10], the sparse ESM technique is used to localize the dominant sources among multiple optical modules rapidly. Also, in [11], an absorbing material is utilized to mitigate radiation from the identified sources.

Another problem with large amounts of radiators in a complex system is the required hardware and testing time for EMC regulation tests. Hence, the authors in [12, 13] derived a mathematical relation using statistical analysis to fast predict the maximum radiation from a large system with numerous similar sub-systems, with a level of certainty provided. Also, measurements were performed to validate the estimation.

This chapter provides an insightful review of EMI diagnostic approaches in different aspects at high frequencies, including source modeling, coupling path analysis and visualization, EMI mitigation, source localization, and emission level prediction. The remaining sections of this chapter are organized as follows. In Section 2, the EMI coupling path analysis and mitigation approaches for optical modules are elaborated. The emission source microscopy (ESM) algorithm is then introduced and applied to optical modules in Section 3. In Section 4, the method for estimating the emission level from multiple radiators is explained. Finally, a conclusion is provided.

2. EMI coupling paths analysis and mitigation

2.1 Modeling optical sub-assembly (OSA) module

The diagram of a typical optical link is shown in **Figure 1** [1]. The cage connector and the transceiver module are enclosed by the connector shield cage located on the line card PCB. The cage connector, through which the signal is transmitted, connects the line card PCB and the transceiver circuit board. The signal sent to the transceiver circuit board is further transmitted to the silicon photonic subassembly. The electrical-to-optical (and vice versa) interface assembly converts the electrical signal into an optical signal, which is subsequently transferred to other devices through an optical fiber cable. The cage connector, the optical transceiver module,

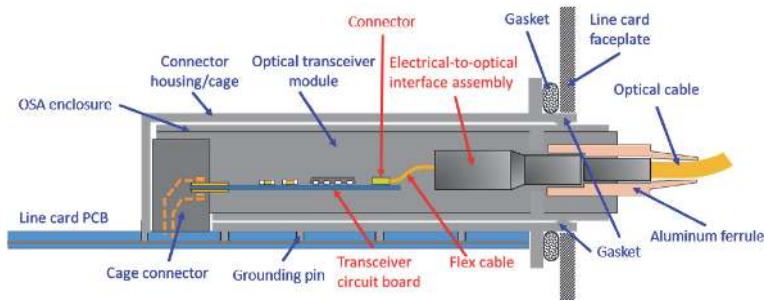


Figure 1.
 Structure diagram of the optical transceiver module [1].

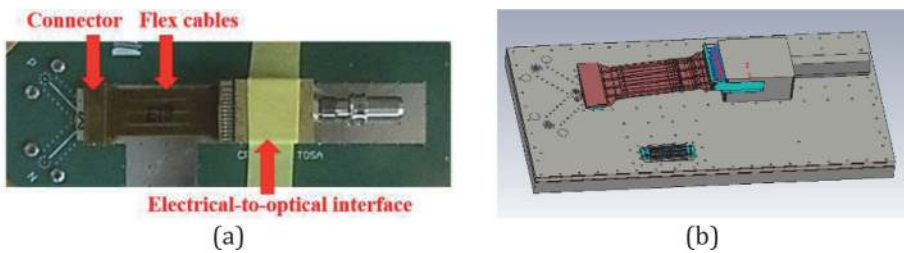


Figure 2.
 Optical sub-assembly test board. (a) Experimental test setup. (b) the corresponding simulation model [1].

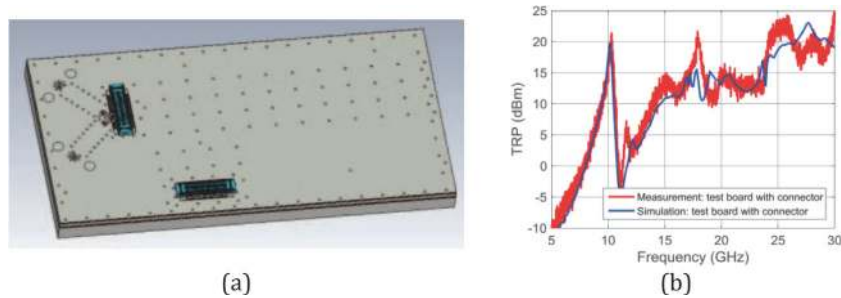


Figure 3.
 (a) The simulation model of the test board with the connector only. (b) TRP comparison between measurement and simulation for the test board with the connector only [2].

and the optical cable ferrule were identified as the primary radiation contributors [3, 4]. The aluminum ferrule surrounding the optical fiber cable forms a radiating antenna that is causing the most EMI problems in meeting regulatory requirements for optical transceiver modules.

The optical sub-assembly (OSA) module was modeled in full-wave simulations [2]. The real structure and simulation model for the OSA module is shown in **Figure 2**. There are mainly three parts in the OSA module to be investigated: the connector, the flex cables, and the electrical-to-optical interface assembly. Firstly, the simulation model for the OSA module needs to correlate well with measurements. The adopted strategy [2] was to gradually increase the model complexity and verify the model accuracy step by step. TRP comparison was used for model validation. **Figures 3–5** show the TRP comparison between simulation and measurement for different models. In **Figure 3**, only the connector was kept. In **Figure 4**, the flex cables were included in the model. The entire OSA module was considered in **Figure 5**.

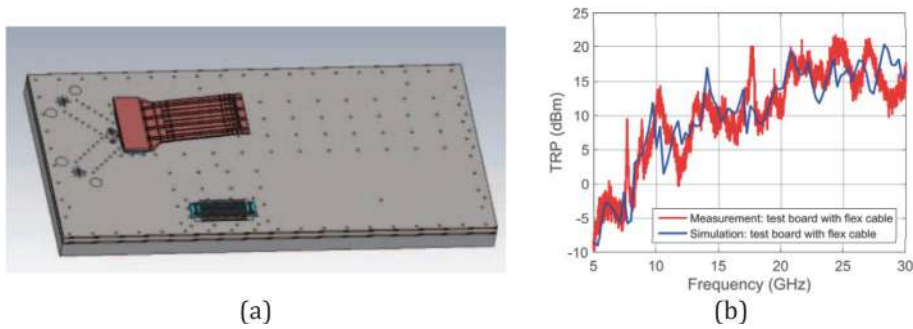


Figure 4. (a) The simulation model of the test board with the long flex PCB. (b) TRP comparison between measurement and simulation for the test board with the long flex PCB [2].

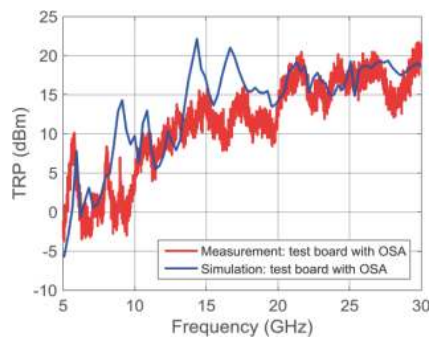


Figure 5. TRP comparison between measurement and simulation for the test board with OSA model as shown in Figure 2 [2].

In Figures 3–5, the TRP results of simulation and measurement agree reasonably well, indicating the accuracy of the simulation model. Several experiments were designed to quantify the contributions from different parts of the model by utilizing an absorbing material [2], as shown in Figure 6. This systematic investigation concludes that the connector and the flex cables are two dominant radiation sources above 10 GHz. In comparison, the electrical-to-optical interface assembly has little contribution to the radiation.

In the OSA module, the connector and the flex cables were diagnosed as the primary radiation contributors above 10 GHz. The structure of the entire optical transceiver module is shown in Figure 7, including the OSA module and an enclosure. There are two individual modules in each optical transceiver module – a transmitter optical subassembly (TOSA) and a receiver optical sub-assembly (ROSA) module. Only the TOSA model will be used for analysis since the interior structure of the ROSA cannot be obtained due to confidentiality. A simulation model was built to place the OSA module within an enclosure to mimic the actual design and analyze the coupling paths from the OSA module to the external EMI radiation. This type of optical transceiver module has two working modes at 25.78 GHz and 27.95 GHz. The following EMI analysis will concentrate on 25.78 GHz. The mechanism at 27.95 GHz is similar to 25.78 GHz and hence is omitted.

2.2 Coupling paths analysis by simulations

Figure 8(a) shows a simulation model in which an OSA module is inserted into a shielding enclosure without the enclosure top. One signal trace was excited with a

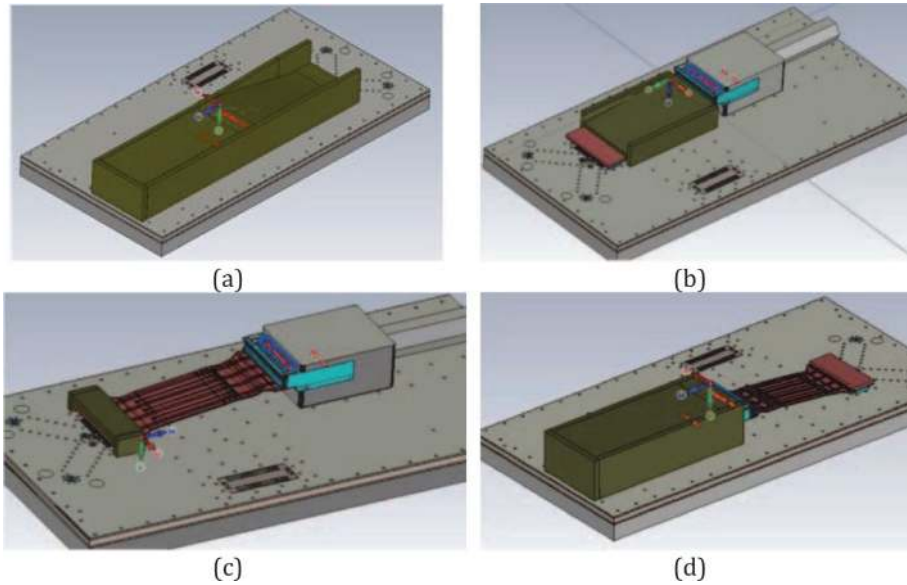


Figure 6. Use absorbing material to cover different parts of the OSA module to determine their contribution to the radiation. (a) the entire OSA module. (b) the flex cables. (c) the connector. (d) the electrical-to-optical interface assembly [2].

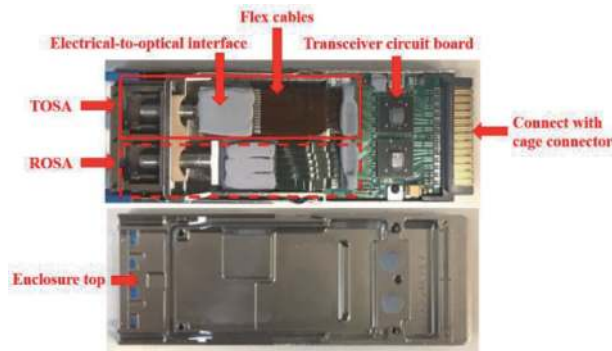


Figure 7. Structure diagram of the optical transceiver module [1].

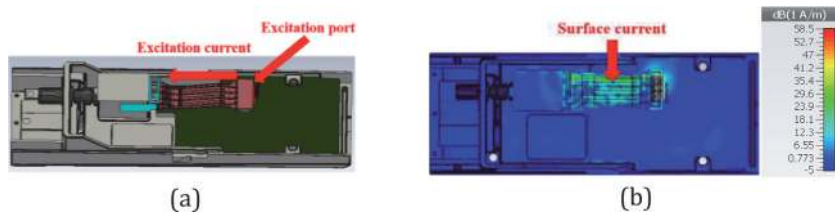


Figure 8. (a) OSA simulation model only without the enclosure top. (b) Surface current distribution at 25.78 GHz in top view [1].

lumped port. The surface current under this circumstance is plotted in **Figure 8(b)**. The surface current is mainly distributed over the connector and the flex cables, as expected. There is little current on the electrical-to-optical interface assembly. It does not contribute to the radiation of the OSA module, which has been validated by applying absorbing materials.

Subsequently, an enclosure was added to the model in **Figure 8**, as shown in **Figure 9**. The right end of the module in **Figure 7** is inserted into a cage connector on a line card. The leakage near the cage connector is negligible compared to the leakage from the optical fiber cable in the front. Therefore, in the simulation model **Figure 9(a)**, the enclosure end that should be connected with a line card was shielded with PEC. In this manner, the coupling path and radiation from the optical output end can be focused on and studied.

As illustrated by **Figure 9(b)**, there is a gap between the cylindrical metal port and the enclosure. The optical fiber cable is connected to this port. Moreover, a mechanical handle insertion area has a small gap and can also potentially cause EMI leakage. Experimental work proved these gaps to be the primary leakage points, as will be introduced later.

After the enclosure top is added to the simulation model, the surface current distributions are plotted in **Figure 9(c)–(e)**. Compared to the current distribution in **Figure 8(b)**, more current appears in the other places, including the enclosure, the electrical-to-optical interface assembly, and the cylindrical metal port that egresses the shielding enclosure. In **Figure 9(e)**, an evident radiation leakage can be observed from the gap. The simulation comparison between **Figure 9** and **Figure 8** demonstrates that “the enclosure cavity provides an EMI coupling path for propagating modes that can illuminate slots and seams in the OSA enclosure” [1]. The aluminum ferrule of the optical fiber cable inserted into the TOSA port forms a monopole antenna that can be efficiently excited with the current leakage. Typically, a network equipment system has tens of or even hundreds of such monopole antennas, which can cause severe EMI issues in meeting compliance requirements.

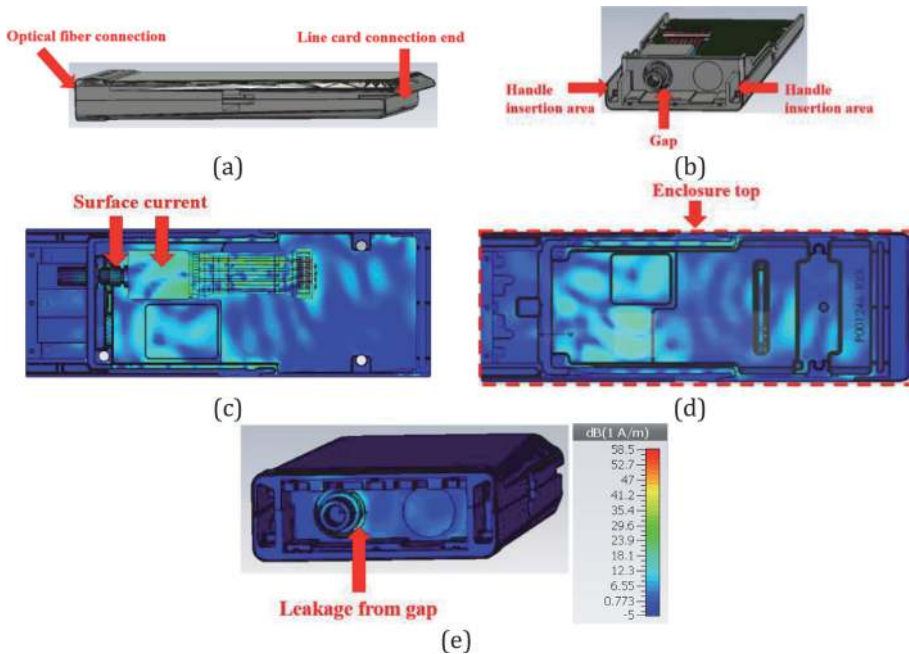


Figure 9. (a) A simulation model for the optical transceiver module, enclosed in a complete enclosure. (b) the positions of the handle insertion area and the gap between the cylindrical metal part and the enclosure. (c) Surface current distribution on the OSA module and the enclosure bottom at 25.78 GHz, with the enclosure top being hidden. (d) Surface current distribution on the OSA module and the enclosure top at 25.78 GHz, with the enclosure bottom being hidden. (e) Surface current distribution on the enclosure surface in front view at 25.78 GHz [1].

2.3 EMI mitigation of optical transceiver modules

The primary radiation sources and the dominant coupling paths have been determined by using simulation and measurement techniques. In this section, mitigation approaches will be proposed correspondingly to suppress the radiation leakage in both simulation and measurement. The effectiveness of the mitigation methods will, in turn, validate the analyzed coupling paths.

2.3.1 EMI mitigation in simulation

Figure 10 shows simulation models with absorbing material being placed at different locations. **Table 1** compares the simulated TRP for the models in **Figure 10** at 25.78 GHz and 27.95 GHz. After adding absorbing material above the flex cables on the underside of the enclosure lid, a TRP reduction of 4–7 dB is achieved at the two frequencies. The TRP is further reduced by 2–3 dB by adding absorbing material to the cylindrical egress of the electrical-to-optical module and the handle insertion areas. Adding absorbing material on the metal surface of the electrical-to-optical module and the cylinder can significantly reduce the TRP by 8–9 dB.

2.3.2 EMI mitigation in measurement

One chassis with functioning optical transceiver modules did not meet the FCC Class A limit plus a required margin at 25.78 GHz and 27.95 GHz in an EMC test. For example, one measurement showed that one line card with four optical transceiver modules passed the FCC Class A limit by 0.4 dB with no margin typically required in EMC regulations. Based on the analysis result of the dominant coupling paths, some mitigation approaches were implemented in the measurement to suppress the EMI radiation and meet the FCC Class A limit with more margins.

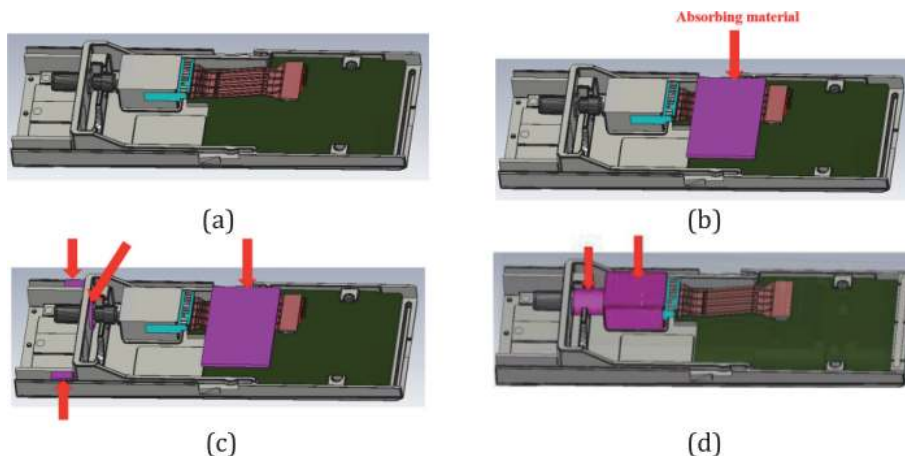


Figure 10.

(a) A simulation model with closed enclosure (enclosure top being hidden) and without absorber. (b) a simulation model with a sealed enclosure, an absorbing material of 26 mm × 16 mm, and a thickness of 1 mm on the enclosure lid underside above the flex cables. (c) a simulation model with a closed enclosure, with absorbing material of 1 mm thickness on the enclosure top above the flex cables, and to the space between the cylindrical metal part of the electrical-to-optical module and the enclosure, as well as the leakage space on the two handle sides of the enclosure. (d) a simulation model with a closed enclosure and absorbing material with a thickness of 0.5 mm on the metal of the electrical-to-optical interface assembly and the metal cylinder inside the enclosure [1].

Simulated TRP (dBm)	25.78 GHz	27.95 GHz
Model in Figure 10(a)	-14.9 dBm	-17.3 dBm
Model in Figure 10(b) (Compared to Figure 10(a))	-22.5 dBm (7.6 dB reduction)	-21.3 dBm (4 dB reduction)
Model in Figure 10(c) (Compared to Figure 10(a))	-25.3 dBm (10.4 dB reduction)	-23.0 dBm (5.7 dB reduction)
Model in Figure 10(d) (Compared to Figure 10(a))	-24.0 dBm (9.1 dB reduction)	-25.3 dBm (8 dB reduction)

Table 1.
TRP simulation results of **Figure 10** [1].

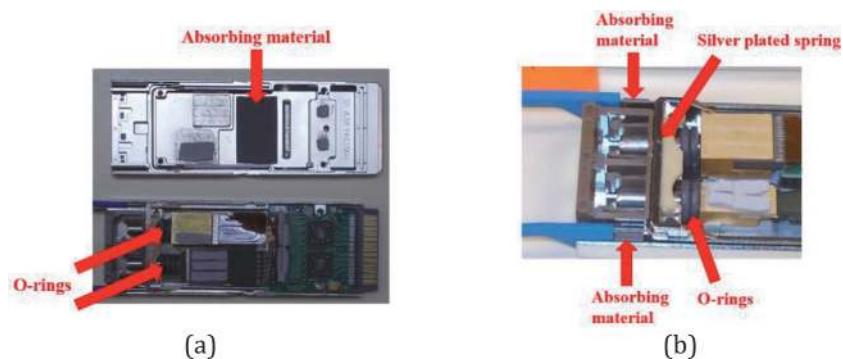


Figure 11.
EMI mitigation methods in the production hardware. (a) Adding absorbing material inside the enclosure above the flex cables and adding grounding O-rings around the cylindrical metal portion of the electrical-to-optical module. (b) Adding some silver-plated spring around the cylindrical metal and adding absorbing material on the handles on two sides [1].

Difference with FCC Class A limit (dB)	25.78 GHz	27.95 GHz
Adding absorbing materials + O-rings (2 line cards, 8 modules)	-8 dB	-4 dB
Adding absorbing materials + O-rings + silver plated spring seal + absorbing materials on handles (2 line cards, 8 modules)	-15 dB	-9 dB

Table 2.
Mitigation of radiated emissions [1].

Figure 11 shows some mitigation methods, such as adding absorbing material, O-rings, and silver-plated spring. **Table 2** shows the EMC test results after applying the mitigation solutions on two line cards with eight optical transceiver modules. Compared with the FCC Class A limit, the largest margin is increased to 15 dB after implementing the mitigations. This outcome corroborates the EMI coupling paths and the mitigation approaches discussed earlier.

A systematic approach has been elaborated to investigate the EMI coupling paths in an optical transceiver module. The procedure includes building simulation models, identifying the dominant radiation modules, analyzing EMI coupling paths through simulations, and finally validating the coupling paths by mitigation in measurements.

The EMI coupling paths in the optical transceiver module can be concluded as follows. The cage connector [4], the connector between the transceiver circuit board and the flex cables, and the flex cables are the dominant radiation sources [1].

The module enclosure provides a cavity-like structure for the propagating modes to radiate from the gap between the electrical-to-optical module and the enclosure. The aluminum ferrule surrounding the optical fiber can be excited with the leakage current and radiate efficiently like a monopole antenna. **Figure 12** illustrates the concluded coupling paths. For a large equipment rack, the EMI can violate regulatory limits with many tens or hundreds of such modules. Mitigation approaches such as absorbing material and elastomer O-rings can effectively suppress EMI radiation in the actual product applications.

2.4 EMI coupling paths visualization

2.4.1 Definition of EM energy parcels

The simulation method in [1] demonstrated the coupling paths, but it did not directly show the coupling paths. Li *et al.* [14, 15] proposed a concept to intuitively visualize coupling paths by utilizing the analogy between the flow of EM energy and fluid flow. The flow of EM energy can be imagined as a certain amount of energy parcels propagating in space. The EM energy flow is defined by the Poynting vector, meaning that the EM energy flow follows the law of conservation of energy. Eq. (1) defines the instantaneous velocity of EM energy parcels.

$$\vec{v}(m/s) = \frac{\vec{S}(J/m^2s)}{u(J/m^3)}, \quad (1)$$

where Vector S represents the instantaneous Poynting vector and is given by Eq. (2), and u means the total magnetic and electric energy density defined by Eq. (3).

$$\vec{S} = \vec{E} \times \vec{H}. \quad (2)$$

$$u = \mu \frac{\vec{H} \cdot \vec{H}}{2} + \epsilon \frac{\vec{E} \cdot \vec{E}}{2}. \quad (3)$$

The time-averaged velocity of the energy parcels is defined as Eq. (4), which is a constant value.

$$\vec{v}_{av} = \frac{\vec{S}_{av}}{u} = \frac{\text{Re}[\vec{S}]}{u}. \quad (4)$$

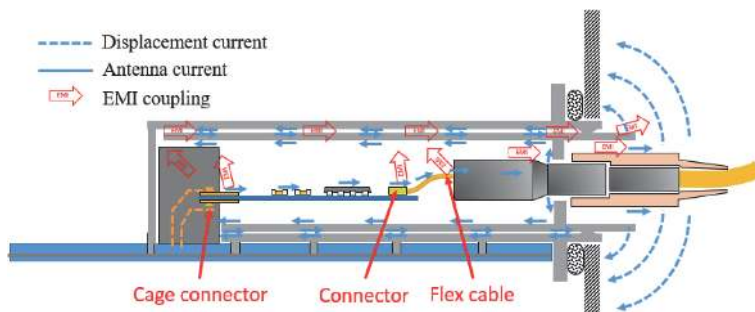


Figure 12. Summary of the EMI coupling paths in the optical transceiver module [1].

Therefore, the trajectory of the energy parcels can be acquired by calculating the streamline (tangential line) of the real part of the complex Poynting vector [14, 15]. The trajectories are tracked back from the receiver antenna to visualize the energy path from the transmitter to the receiver.

2.4.2 Apply coupling path visualization to optical modules

Some researchers applied the trajectory concept of energy parcels to visualize the EMI coupling paths on quad form-factor pluggable (QSFP) modules and propose corresponding mitigation approaches [5, 6]. In [5], an EMI issue related to a QSFP module possessing a heatsink was studied. The issue is that when an optical module is inserted, the heatsink on top of the optical module rises. Thus an air gap is created by the rising heatsink, and the shielding effectiveness (SE) of the QSFP shielding cage is degraded. **Figure 13** describes the measurement setup to quantify the SE of the QSFP shielding cage. There were two reverberation chambers (RC): one side is noisy, and the other side is quiet. A transmitter (Tx) antenna and a receiver (Rx) antenna were placed on the noisy and quiet sides, respectively.

The potential coupling paths related to the rising heatsink are depicted in **Figure 14**. The rising heatsink provides a guiding structure for the propagating waves. The EM waves can penetrate the cage from the path between the heatsink and the cage. This path around the cage guides the EM waves through the cage. Besides, there is a small gap between the cage and the line card PCB so that EM waves can go through the cage from the bottom.

The concept of energy parcels and their trajectories was applied to validate the above hypothesis about the coupling paths [5]. The result of the trajectories is shown in **Figure 15**. It can be observed that the rising heatsink behaves as a guided

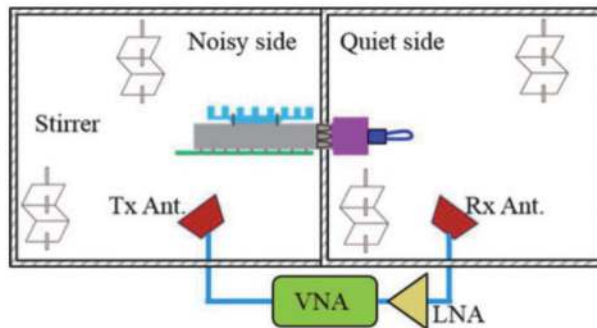


Figure 13. Measurement setup for the shielding effectiveness of the optical module [5].

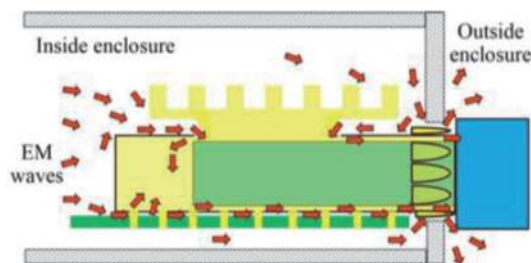


Figure 14. Potential coupling paths when there is a heatsink [5].

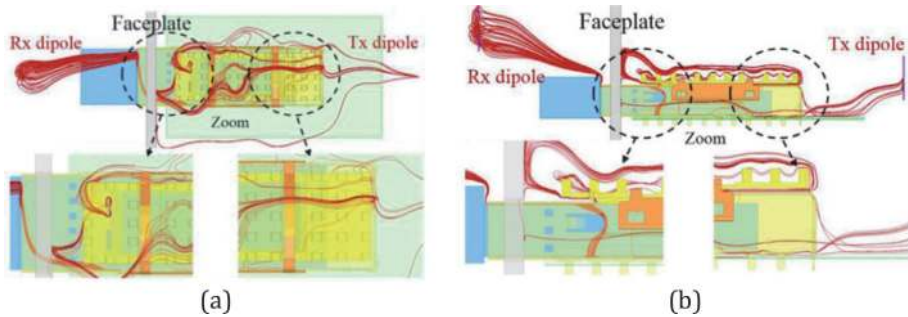


Figure 15. Reversed tracked energy parcels from the receiver antenna (Rx) to the transmitter antenna (Tx). (a) Top view. (b) Side view [5].

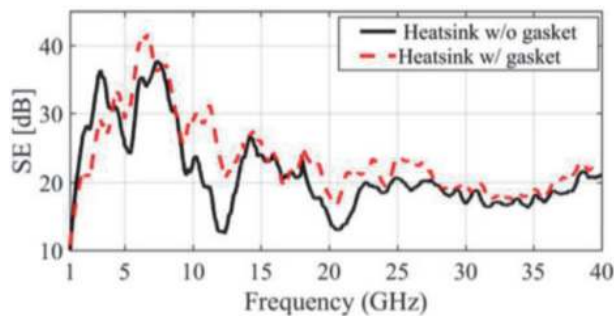


Figure 16. Comparison between the averaged SE of the cage with and without the gasket [5].

structure for the propagating waves, and the area between the heatsink and the top of the cage contributes as a leakage path.

According to the analysis result using the coupling path visualization, a mitigation approach was applied by placing a window frame gasket between the cage and the heatsink [5]. The change of SE is plotted in **Figure 16**. The SE of the QSFP shielding cage is notably improved by a few decibels over the entire frequency range. This improvement corroborates the EMI coupling paths concluded from the trajectory visualization of energy parcels. Similarly, the same approach was adopted in [6] to investigate the coupling paths for flyover QSFP connectors. Also, corresponding mitigation methods using an absorbing material were demonstrated to work effectively.

3. Emission source microscopy (ESM)

The emission source microscopy (ESM) method [9] can identify far-field radiation sources by scanning the far field over a plane above a device under test (DUT) and back-propagating the field onto the DUT plane to localize the dominating sources. Both the field magnitude and phase are required for the back-propagation calculation. Therefore, phase measurement is needed. A typical way of measuring the field phase from an active DUT is shown in **Figure 17**. Antenna B is the reference antenna with a fixed location for phase measurement. Antenna A is the scanning antenna that moves with a scanning robot to acquire the field information at different locations. Antenna A and B are connected to the channel A and B of a vector network analyzer (VNA). The VNA operates at the tuned receiver mode and

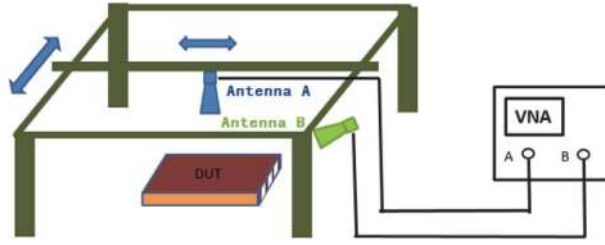


Figure 17.
ESM system setup [10].

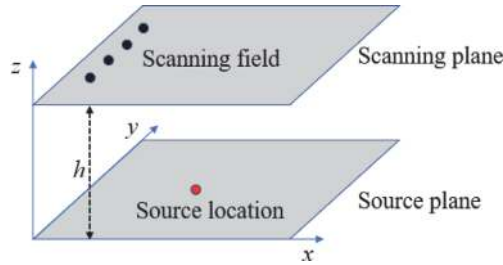


Figure 18.
Diagram of ESM algorithm.

receives signals at channels *A* and *B* simultaneously. The phase difference between *A* and *B* is used as the field phase, while the signal magnitude received by channel *A* is the field magnitude.

3.1 Algorithm description

Figure 18 illustrates the ESM algorithm. There is a scanning plane and a source plane, which are parallel to the *x*-*y* plane. The distance between them is *h*. The far field, including magnitude and phase, is collected on the scanning plane. Suppose that $E_t(x, y, h)$ is the tangential field on the scanning plane, and $E_t(x, y, 0)$ is the tangential field on the source plane. The mathematical calculation of the ESM algorithm [9] can be summarized by Eq. (5).

$$E_t(x, y, 0) = F^{-1}\{F[E_t(x, y, h)] \cdot e^{jk_z h}\}, \quad (5)$$

where $k_z = \sqrt{k^2 - k_x^2 - k_y^2}$ is the *z* component of the propagation vector if $k_x^2 + k_y^2 \leq k^2$; $k_z = j\sqrt{k_x^2 + k_y^2 - k^2}$ if $k_x^2 + k_y^2 > k^2$; k_x and k_y are the spatial frequencies of 2D Fourier transform; F and F^{-1} are the forward and reverse 2D Fourier transform operators, respectively. The basic idea behind this ESM method is to decompose the scanning field into plane waves with different propagation vectors in *x*, *y*, and *z* directions.

In [11], an electronic system with multiple physical layer transceivers was diagnosed using the ESM method. The source location at a frequency of interest was precisely localized. Afterward, by applying an absorbing material to the identified source location, the radiated power at the corresponding frequency was effectively suppressed.

3.2 Sparse ESM

Using the original ESM method [9], dense and uniform scanning samples are needed, which is time-consuming and inefficient in fast EMI diagnostic applications. Therefore, a sparse ESM method [10] was proposed to improve the scanning speed using sparse samples. Even though background noise is introduced to the reconstructed images, the scanning time is significantly reduced. Mathematical derivations show that the signal-to-noise ratio (SNR) of the reconstructed images is proportional to the number of sparse samples. Thus, the dominant radiation sources can be identified using an appropriate number of scanning points.

The sparse ESM method can locate dominant sources, but the absolute field strength of the reconstructed images is not trustable. More sparse samples will increase the field magnitude of the reconstructed images due to the mathematical process of Fourier transform. To tackle this limitation, a nearest-neighbor interpolation method [10] was adopted to interpolate the scanning field and calculate the radiated power from the sources. **Figure 19** shows an example of the nearest-neighbor interpolation method. According to the sparse samples, the scanning domain is segmented into multiple polygon areas, and each polygon represents the area closest to one scanning sample. Afterward, the radiated power through the scanning plane can be calculated according to Poynting's theorem expressed in Eq. (6) [10].

$$P_{tot} = \iint_A \frac{|\vec{E}|^2}{2\eta} \cdot dS = \sum_i \frac{|\vec{E}_i|^2}{2\eta} \cdot A_i, \quad (6)$$

where η is the free space wave impedance; \vec{E}_i is the field at sampling location i ; A_i is the area of the corresponding nearest-neighbor region.

To validate if radiated power can be accurately calculated, an experiment was performed [10] using the setup in **Figure 20**. Two horn antennas were utilized as the transmitter and receiver, respectively. Antenna B was at a fixed position, and Antenna A was moved manually through a scanning robot to obtain the radiated field of Antenna B . Assume that the main beam of Antenna B is narrow, which is true in most cases. The scanning plane is sufficiently large compared with the main beam of Antenna B . Hence, the radiated power of Antenna B can all propagate through the scanning plane. Moreover, the polarization direction of Antenna A and B are aligned with each other. Thus, it is reasonable to expect that the radiated

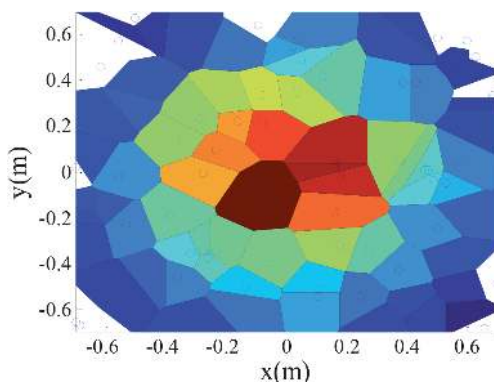


Figure 19.
 An example of the nearest-neighbor interpolation [10].

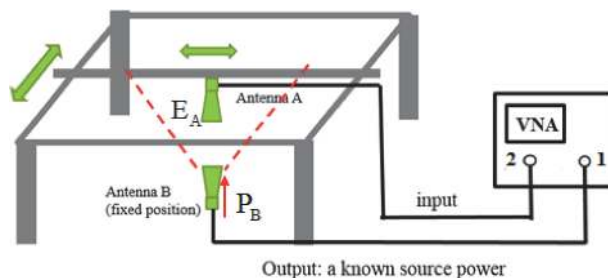


Figure 20. Measurement setup for validating the nearest-neighbor interpolation method in calculating the radiated power [10].

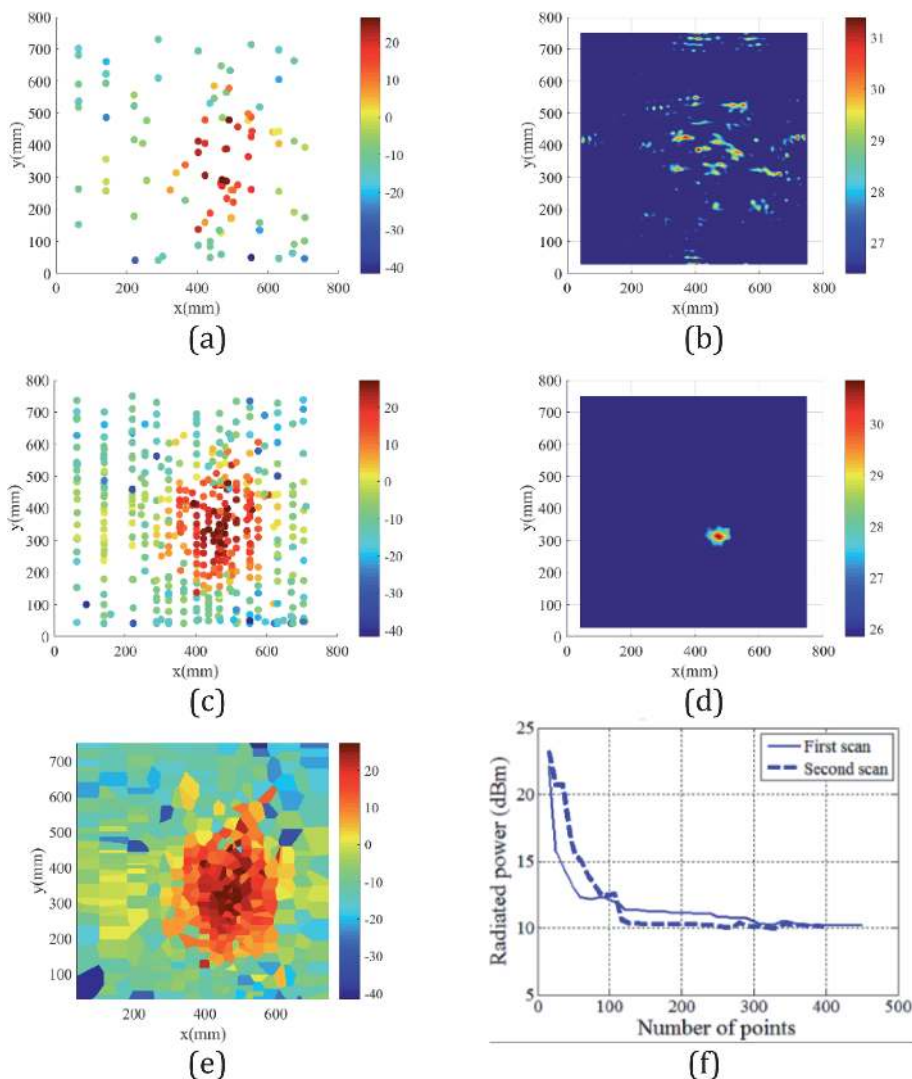


Figure 21. (a) Scanning samples when $N = 100$. (b) Reconstructed image when $N = 100$. (c) Scanning samples when $N = 454$. (d) Reconstructed image when $N = 454$. (e) E field magnitude on the scanning plane after using nearest-neighbor interpolation when $N = 454$. (f) the convergence of calculated radiated power as a function of the number of samples [10].

power of Antenna *B* can be all captured by Antenna *A* using the nearest-neighbor interpolation method.

A vector network analyzer (VNA) was utilized to measure the scanning field through S_{21} as shown in **Figure 20**. The measured E field values of Antenna *A* can be obtained through the antenna factor of Antenna *A*. If the incident voltage of Antenna *B* is 1 V, the incident power of Antenna *B* will be calculated as 10 dBm in a 50- Ω transmission line system. In other words, the expected radiated power calculated using the nearest-neighbor interpolation method is 10 dBm.

Figure 21 presents the measurement process using the measurement setup in **Figure 20**. With the increase of sampling number, the quality of the reconstructed image is also improved according to the conclusion in [10]. **Figure 21(e)** shows the scanning field after using the nearest-neighbor interpolation method. **Figure 21(f)** plots the convergence of the calculated radiated power for two different scans, which both converged to 10 dBm as expected. This experiment demonstrates that the sparse ESM method can locate dominant radiation sources and estimate radiated power by sparse scanning samples.

3.3 Apply ESM to optical transceiver modules

Optical transceiver modules are widely used in Gigabit Ethernet systems to transmit high-frequency data of several hundred gigabits per second (Gbps). Serious EMI problems can be caused at high frequencies by a large number of these modules. EMI diagnostics of multiple potential radiation modules is troublesome. The sparse ESM method introduced earlier is a valuable tool to locate radiation sources efficiently and quantify radiated power. In this section, the sparse ESM method is applied to diagnose multiple optical transceiver modules. **Figure 22** shows a real-world DUT with 16 optical transceiver modules, which generate 15 distinct radiation peaks around 10.3125 GHz. The frequency peak # 11 was selected in this measurement. The sparse ESM was adopted to identify the optical transceiver module that caused frequency # 11 among the 16 modules.

A zero span of a VNA was used, as explained in [9], to focus on frequency # 11. The field magnitude and phase on a scanning plane were measured using the VNA tuned-receiver mode, as illustrated in **Figure 17**. **Figure 23** shows the measured field, reconstructed image, and calculated radiated power. The total number of scanning samples was 352.

In **Figure 23(b)**, the reconstructed source image has a clear hotspot corresponding to the location of one pair of optical transceiver modules. Interestingly, as shown in **Figure 23(c)**, the reconstructed field phase shows a series of phase contours surrounding the corresponding source location. Even though the sampled scanning field was obtained sparsely, the reconstructed image has a

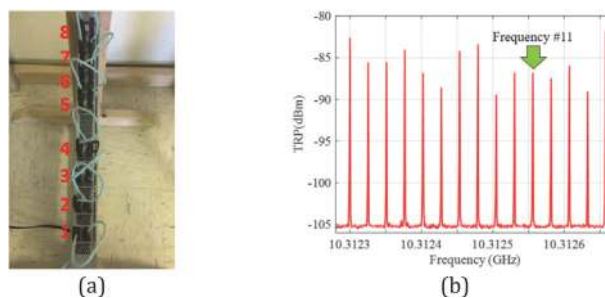


Figure 22.
(a) Validation DUT with 16 optical transceiver modules (numbered by pairs). (b) 15 radiation peaks from the DUT around 10.3125 GHz [10].

continuous distribution due to Fourier transform and inverse Fourier transform in Eq. (1). **Figure 23(d)** shows the convergence of radiated power as more scanning points were sampled. The converged radiated power is approximately -83.4 dBm.

One more experiment was implemented to validate the identified radiation module in **Figure 23** by removing radiation pair # 3 from the DUT and performing another ESM scan. The result is shown in **Figure 24**. The measured scanning field, the reconstructed source field, and the calculated radiated power were significantly reduced. After removing the radiation module for frequency # 11, there is some radiation from the same location. The reason is that the physical layer interface IC beneath the optical module is still radiating.

Furthermore, the total radiated power (TRP) for the two cases in **Figures 23** and **24** was measured in a reverberation chamber (RC) for comparison, and the result is listed in **Table 3**. After removing radiated pair # 3, the TRP value is reduced by 14.1 dB, which is close to the 13.5 dB reduction estimated by the sparse ESM scanning.

The above experiments demonstrate that the sparse ESM is a reliable technique to identify the locations and quantify the radiated power of dominant sources at high frequencies. As a commonly used product in data communication systems, optical transceiver modules were used as the DUT. The sparse ESM method can be applied to identify the radiating modules rapidly.

However, the measurement for the sparse ESM method mentioned above was performed manually, which was user-unfriendly. Also, the image quality can be degraded by operators' subjective decisions and perceptions. An approach based on Gaussian process regression was proposed to achieve automatic scanning to address this issue [16]. The Gaussian process is used to estimate the amplitude variation of the scanned field and its uncertainty to focus on the most relevant scanning area. Thus, compared with pure random scanning, the proposed approach can save the number of scanning samples.

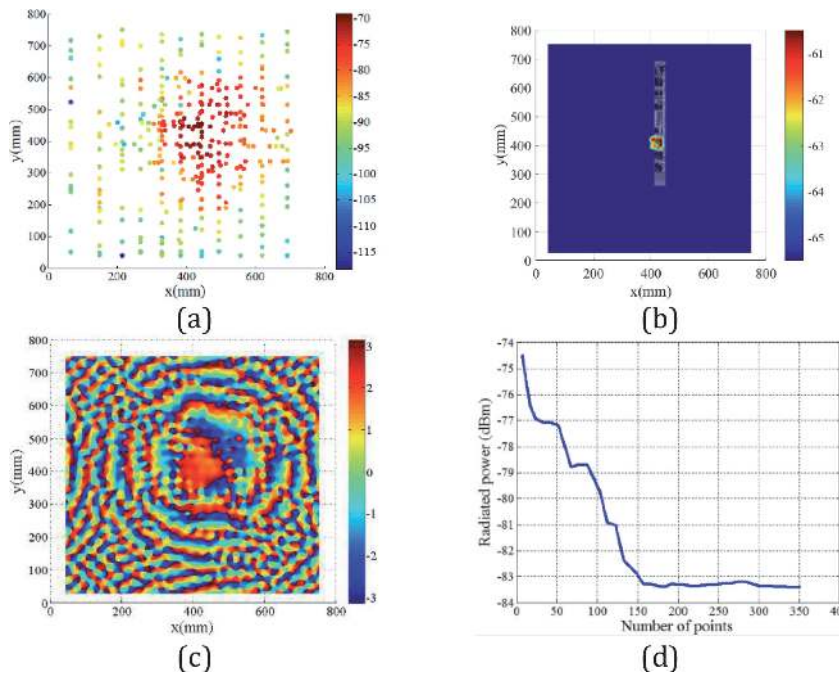


Figure 23. Scanning result at frequency # 11. (a) E field on the scanning plane. (b) the magnitude of the reconstructed image on the DUT plane. (c) the phase of the reconstructed image on the DUT plane. (d) the convergence of calculated radiated power [10].

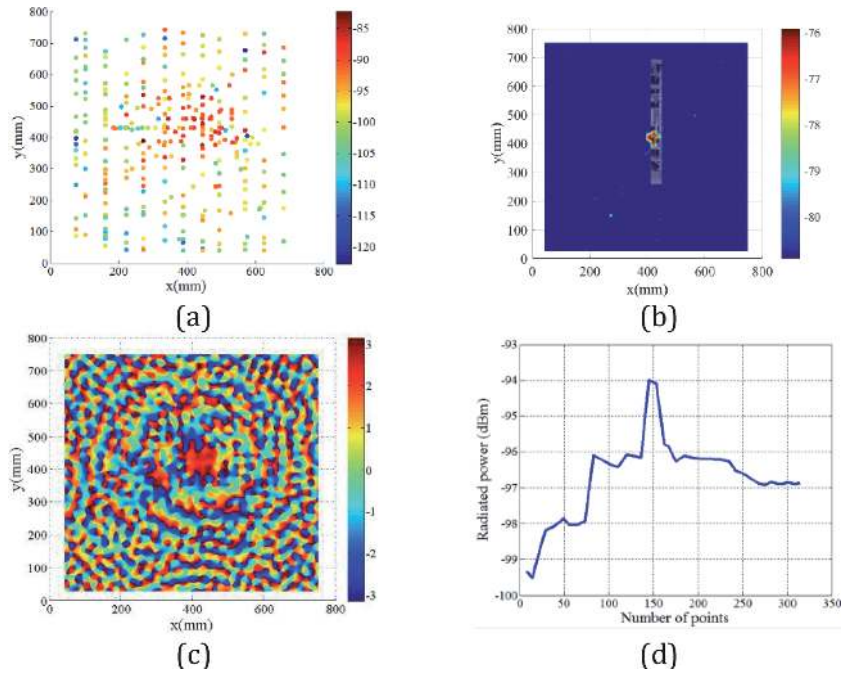


Figure 24. Scanning result at frequency # 11 after removing the corresponding radiated pair # 3. (a) E field on scanning plane. (b) the magnitude of the reconstructed image on the DUT plane. (c) the phase of the reconstructed image on the DUT plane. (d) the convergence of calculated radiated power with the increase of the number of samples [10].

Power values	Power estimation through interpolation	TRP measured in an RC
Power with pair # 3 (dBm)	-83.4	-86.9
Power without pair # 3 (dBm)	-96.9	-101.0
Power reduction (dB)	13.5	14.1

Table 3. Power comparison at frequency # 11 [10].

4. Multiple EMI radiators

Measuring the maximum E field emission for a complex system with numerous optical modules requires exhaustive hardware testing. **Figure 25** illustrates a large network router with many optical modules. The 3D radiation pattern of a single optical module was measured as depicted in **Figure 25(b)**. Statistical analysis and simulation were then performed to fast estimate the E field emission from multiple radiators without running actual hardware testing [12, 13].

The phased array antenna theory and Monte Carlo simulation were utilized to perform the statistical analysis [12]. A tendency of $10\log N$ (dB) was found for the maximum electric field emission from a system with radiators at the same frequency with random phase distribution, where N is the number of radiators. Also, it was found that when multiple radiators with the same magnitude and random distribution contribute simultaneously, the maximum E field follows a normal distribution. Hence, a cumulative distribution function (CDF) can be obtained, and a level of certainty for the E field estimation can be provided.

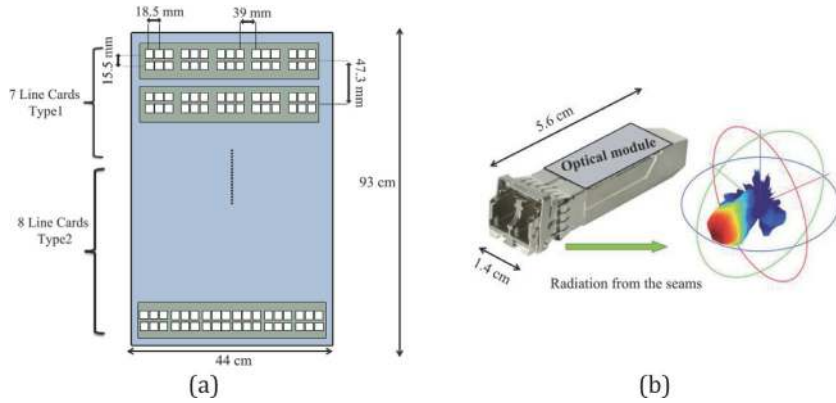


Figure 25. (a) A large network router consisting of numerous optical modules radiating at 10.31 GHz. (b) a typical optical module and its 3D radiation pattern from the seams [12].

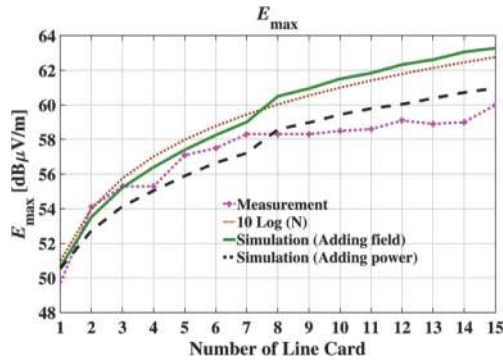


Figure 26. E_{max} comparison between measurement and prediction as the number of line cards increases [12].

Figure 26 compares the E_{max} between the measurement, simulation, and estimation when the number of line cards increases. “Adding field” means using the same frequency for all line cards, while “adding power” means using different frequencies for each line card. It is shown in **Figure 26** that adding power intensities instead of adding fields has a slower slope than $10\log N$ (dB) tendency. From **Figure 26**, it can be concluded that the simulation and measurement results can agree reasonably well with the $10\log N$ (dB) tendency. When the number of line cards increases, the measurement result starts to deviate slightly from the estimation. The reason given in [12] is that more line cards meant a higher probability of missing the maximum electric field in the measurement, depending on the radiation pattern of the receiving horn antenna.

More experiments were implemented in [13] to validate the $10\log N$ tendency by using patch antennas to mimic the radiation of optical modules. The same agreement between measurement and estimation was observed. **Figure 27** shows the CDF distribution for 15 and 30 patch antennas with random phase excitation. The measured E_{max} under different phase randomizations fell into the 40–90% range. Therefore, it can be concluded from the experiment that the statistical model can reliably estimate the worst E field emission from multiple radiators with random phase distribution. By adopting the $10\log N$ (dB) tendency and the CDF of normal distribution, one can easily estimate the likelihood of passing an EMC regulation

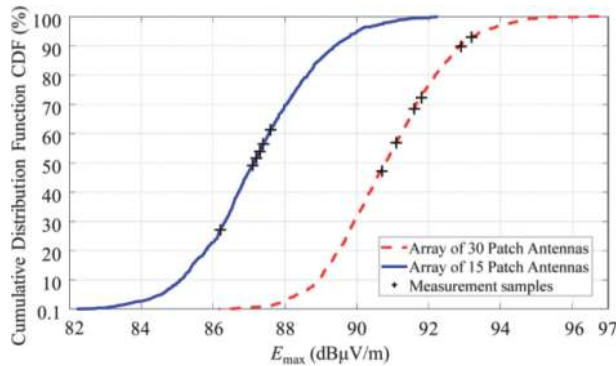


Figure 27. Measurement samples and prediction of the CDF for two different number of patch antennas [13].

without running exhaustive hardware testing with more radiation modules to be installed.

5. Conclusion

In this chapter, some effective diagnostic approaches for industrial products at high frequencies are reviewed. First, the study of an explicit optical transceiver module is presented to investigate the internal EMI coupling mechanism. An accurate simulation model for the optical subassembly (OSA) module was constructed by correlating the total radiated power of simulation and measurement. More simulations and measurements were performed to identify the dominant radiation modules and coupling paths. An intuitive visualization method for EMI coupling paths was also adopted. According to the EMI coupling paths, mitigation solutions were correspondingly proposed and demonstrated to work effectively in real product applications. Subsequently, an emission source microscopy (ESM) method that can efficiently localize far field radiation sources is introduced. Using the ESM technique, the dominant radiation modules among multiple optical modules can be rapidly identified. Moreover, for numerous sources radiating at the same frequency with random phase distribution, the maximum electric field emission has a $10\log N$ (dB) tendency, where N is the number of sources. Thus, the probability of passing an EMC regulation can be fast estimated without running exhaustive hardware testing. This chapter reviews and summarizes an insightful and systematic approach for high-frequency EMI diagnostics for industrial products.

Acknowledgements

The authors would like to thank Prof. James Drewniak, Prof. David Pommerenke, Prof. Victor Khilkevich, Dr. Kyoungchoul Koo, Dr. Jing Li, Dr. Alpesh Bhoje, Xiao Li, Xiangyang Jiao, and Sukhjinder Toor for their kind help and support on the related research.

Conflict of interest

The authors declare no conflict of interest.

Author details


Ling Zhang^{1*}, Yuru Feng¹, Jun Fan² and Er-Ping Li¹

1 Zhejiang University, Hangzhou, China

2 Missouri University of Science and Technology, USA

*Address all correspondence to: lingzhang_linson@qq.com

IntechOpen

© 2021 The Author(s). Licensee IntechOpen. This chapter is distributed under the terms of the Creative Commons Attribution License (<http://creativecommons.org/licenses/by/3.0>), which permits unrestricted use, distribution, and reproduction in any medium, provided the original work is properly cited. 

References

- [1] L. Zhang et al., “EMI Coupling Paths and Mitigation in Optical Transceiver Modules,” in *IEEE Transactions on Electromagnetic Compatibility*, vol. 59, no. 6, pp. 1848–1855, Dec. 2017, DOI: 10.1109/TEMC.2017.2697761.
- [2] J. Li et al., “EMI coupling paths in silicon optical sub-assembly package,” 2016 IEEE International Symposium on Electromagnetic Compatibility (EMC), Ottawa, ON, Canada, 2016, pp. 890–895, DOI: 10.1109/ISEMC.2016.7571768.
- [3] J. Li, S. Toor, A. Bhobe, J. L. Drewniak and J. Fan, “Radiation physics and EMI coupling path determination for optical links,” 2014 IEEE International Symposium on Electromagnetic Compatibility (EMC), Raleigh, NC, USA, 2014, pp. 576-581, DOI: 10.1109/ISEMC.2014.6899037.
- [4] J. Li, X. Li, S. Toor, H. Fan, A. U. Bhobe, J. Fan, and J. L. Drewniak, “EMI Coupling Paths and Mitigation in a Board-to-Board Connector,” in *IEEE Transactions on Electromagnetic Compatibility*, vol. 57, no. 4, pp. 771–779, Aug. 2015.
- [5] A. Talebzadeh, P. C. Sochoux, J. Li, Q. Liu, K. Ghosh, and D. Pommerenke, “Shielding Effectiveness, Coupling Path, and EMI Mitigation for QSFP Cages With Heatsink,” in *IEEE Transactions on Electromagnetic Compatibility*, vol. 60, no. 5, pp. 1254–1262, Oct. 2018, DOI: 10.1109/TEMC.2018.2813889.
- [6] A. Talebzadeh et al., “Coupling Path Visualization and EMI Mitigation for Flyover QSFP Connectors,” in *IEEE Transactions on Electromagnetic Compatibility*, vol. 62, no. 4, pp. 1037–1044, Aug. 2020, DOI: 10.1109/TEMC.2019.2943290.
- [7] D. Baudry, C. Arcambal, A. Louis, B. Mazari, and P. Eudeline, “Applications of the Near-Field Techniques in EMC Investigations,” in *IEEE Transactions on Electromagnetic Compatibility*, vol. 49, no. 3, pp. 485–493, Aug. 2007, DOI: 10.1109/TEMC.2007.902194.
- [8] J. J. H. Wang, “An examination of the theory and practices of planar near-field measurement,” in *IEEE Transactions on Antennas and Propagation*, vol. 36, no. 6, pp. 746–753, June 1988, DOI: 10.1109/8.1176.
- [9] P. Maheshwari, H. Kajbaf, V. V. Khilkevich, and D. Pommerenke, “Emission Source Microscopy Technique for EMI Source Localization,” in *IEEE Transactions on Electromagnetic Compatibility*, vol. 58, no. 3, pp. 729–737, June 2016, DOI: 10.1109/TEMC.2016.2524594.
- [10] L. Zhang et al., “Sparse Emission Source Microscopy for Rapid Emission Source Imaging,” in *IEEE Transactions on Electromagnetic Compatibility*, vol. 59, no. 2, pp. 729–738, April 2017, DOI: 10.1109/TEMC.2016.2639526.
- [11] X. Jiao et al., “EMI mitigation with lossy material at 10 GHz,” 2014 IEEE International Symposium on Electromagnetic Compatibility (EMC), Raleigh, NC, USA, 2014, pp. 150–154, DOI: 10.1109/ISEMC.2014.6898960.
- [12] J. Meiguni et al., “EMI Prediction of Multiple Radiators,” in *IEEE Transactions on Electromagnetic Compatibility*, vol. 62, no. 2, pp. 415–424, April 2020, DOI: 10.1109/TEMC.2019.2914240.
- [13] W. Zhang et al., “System-Level EMI of an Artificial Router System With Multiple Radiators: Prediction and Validation,” in *IEEE Transactions on Electromagnetic Compatibility*, vol. 62, no. 4, pp. 1601–1610, Aug. 2020, DOI: 10.1109/TEMC.2020.3006517.
- [14] H. Li, V. V. Khilkevich and D. Pommerenke, “Identification and

Visualization of Coupling Paths—Part I: Energy Parcel and Its Trajectory,” in IEEE Transactions on Electromagnetic Compatibility, vol. 56, no. 3, pp. 622–629, 1 June 2014, DOI: 10.1109/TEMC.2014.2314645.

[15] H. Li, V. V. Khilkevich and D. Pommerenke, “Identification and Visualization of Coupling Paths—Part II: Practical Application,” in IEEE Transactions on Electromagnetic Compatibility, vol. 56, no. 3, pp. 630–637, 1 June 2014, DOI: 10.1109/TEMC.2014.2314660.

[16] J. Li, J. Zhou, S. Yong, Y. Liu, and V. Khilkevich, “Automatic sparse ESM scan using Gaussian process regression,” 2020 IEEE International Symposium on Electromagnetic Compatibility & Signal/Power Integrity (EMCSI), Reno, NV, USA, 2020, pp. 671–675, DOI: 10.1109/EMCSI38923.2020.9191463.